Photoacoustics 13 (2019) 66–75

Contents lists available at ScienceDirect

Photoacoustics

journal homepage: www.elsevier.com/locate/pacs

Research article

Optimized light delivery probe using ball lenses for co-registered photoacoustic and ultrasound endo-cavity subsurface imaging

Guang Yang[a], Eghbal Amidi[a], Sreyankar Nandy[a], Atahar Mostafa[a], Quing Zhu[a,b,*]

[a] Department of Biomedical Engineering, Washington University in St. Louis, St. Louis, MO 63130, USA
[b] Department of Radiology, Washington University School of Medicine, St. Louis, MO 63110, USA

ARTICLE INFO

Keywords:
Photoacoustic imaging
Optimized light delivery probe
Ball-shaped fiber tip
Adenocarcinoma

ABSTRACT

An optimized hand-held photoacoustic and ultrasound probe suitable for endo-cavity tumor subsurface imaging was designed and evaluated. Compared to previous designs, the prototype probe, consisting of four 1 mm multi-mode optical fibers attached with 1.5 mm diameter ball-shaped fiber tips sandwiched between a transvaginal ultrasound transducer and a custom-made sheath, demonstrated a higher light output and better beam homogeneity on tissue subsurface. The output power and fluence profile were simulated for different design parameters. A camera recorded fluence profiles through calibrated intralipid solution at various imaging depths. The light delivery efficiency was experimentally compared with and without the ball lenses, based on *ex-vivo* imaging of human colorectal cancer and *in-vivo* imaging of a palmar vein proximal to the human wrist. The simulations and experiments demonstrated that ball-shaped fiber tip design can achieve homogeneous fluence distribution on tissue subsurface with acceptable light output efficiency, suggesting its clinical potential for *in-vivo* endo-cavity imaging.

1. Introduction

Adenocarcinoma is a type of cancerous tissue that forms in mucus-secreting glands throughout the body. For example, adenocarcinomas make up around 96% of colorectal cancers, and some cervical cancers (10%) are also adenocarcinomas [1–4]. The depth of invasion for early stage adenocarcinoma is generally around 1 mm to 7 mm. For example, the stromal invasion depth for cervical adenocarcinoma was measured to be 5 mm or less from the base of the epithelium, with a horizontal spread of 7 mm or less by microscopy [5]. Currently, magnetic resonance imaging (MRI) is the best available imaging modality for detecting and surveilling these tumors, however, its resolution is limited, hindering imaging of small malignancies or abnormalities. Computed tomography (CT) and positron emission tomography (PET) are primary modalities for evaluating tumor metastasis, but are limited in their ability to locally stage malignancies [6]. Clearly, a non-invasive imaging technique is needed to provide high tumor contrast at reasonable microscale resolution and clinically relevant depths.

Photoacoustic imaging or tomography (PAI or PAT) is an emerging technique with the potential of providing functional information in biological tissues [7–16]. Optical absorption, the main PAT contrast, is directly related to tumor angiogenesis and tumor hypoxia. Tumor angiogenesis and oxygen consumption are significant indicators for tumor growth, metastasis, and therapeutic response [17,18]. By combining PAT with Ultrasound (US), a PAT/US dual-modality imaging system can simultaneously provide anatomical and functional information about tumors [19–22].Optical fiber-based photoacoustic imaging probes have been designed for various applications by several research groups [23–33]. Linear ultrasound transducer array-based PAT probes with both a dark-field illumination scheme [29–31] and a bright-field scheme [32,33] have also been investigated. However, the large sizes of the US array and the high loss in the light transmission of fiber bundles [28–33] make them unsuitable for endo-cavity PAT/US imaging. Previously, our group had designed several optical fiber-based transvaginal PAT/US imaging probes for ovarian cancer diagnosis [34,35]. In one early study, the probe consisted of 36 fibers, each with a 200 μm core diameter, paired with a custom-made high-power fiber-optic beam splitter assembly that was integrated with a commercial transvaginal ultrasound transducer and housed in a protective shield. However, the custom-made beam splitter was expensive and easily damaged at the splitter junction by the high energy involved. Later designs were modified to use four multi-mode optical fibers with 1 mm core diameters. To eliminate potential hotspots and homogenize the light output of the four fibers, the fibers were enclosed in a custom-designed sheath. The sheath was made of acrylonitrile butadiene styrene (ABS), constructed with a 3D printer, and internally lined with an aluminized

* Corresponding author at: Department of Biomedical Engineering, Washington University in St. Louis, St. Louis, MO 63130, USA.
E-mail address: zhu.q@wustl.edu (Q. Zhu).

https://doi.org/10.1016/j.pacs.2018.12.001
Received 5 October 2018; Received in revised form 23 November 2018; Accepted 6 December 2018
Available online 07 December 2018

film with a reflection coefficient of 85%. The sheath gradually tapered towards the exit end of the probe to allow easy penetration into the body cavity and optimize light homogeneity. In this design, the 8–10 mm thick vagina muscle wall functioned as the light diffuser to homogenize the light beam before it reached the ovary. However, the light beam was not optimized for endo-cavity imaging of surface tumors, such as adenocarcinomas.

The commonly used lens components in fiber-optic microprobes include gradient-index (GRIN) lenses [36,37], drum lenses [38], and fiber fused ball lenses [39,40].

In this paper, we report the optimal design, implementation, and evaluation of an optical fiber-based transvaginal PAT/US imaging probe for endo-cavity imaging of adenocarcinomas. A ball-shaped lens is glued to each of four fiber tips to homogenize the light illumination on the tissue surface. The light delivery system consists of light coupling optics, a custom-made transducer sheath, and four 1 mm core multi-mode optical fibers with a ball-shaped lens glued on their tip. The endo-cavity illumination design was simulated for various numerical apertures (NA), refractive indexes, probe taper angles, and fiber distances from the tip of the probe, and was subsequently validated by experimental measurements.

2. Methods and materials

2.1. Experiment setup and imaging probe

Shown in Fig. 1(a), the co-registered PAT/US system consists of a Ti: sapphire (Symphotics TII, LS-2134, Symphotics, Camarillo, California) optically pumped with a Q-switched Nd:YAG laser (Symphotics TII, LS-2122) to deliver pulsed laser light (10 ns pulse duration, 15 Hz pulse repetition rate, 20 mJ/pulse at 750 nm wavelength). Four fibers receive light from the laser through an optimized illumination system [41]. A commercial US system (EC-12R, Alpinion Medical System, Republic of Korea) is used to acquire the corresponding US and PAT data.

To deliver light to the imaged tissue, the imaging probe was constructed based on the optimal parameters obtained from the simulation. Four 1 mm core multi-mode optical fibers (FP1000ERT, 0.50 NA, THORLABS, n = 1.4 in the 700–800 nm wavelength range) were housed in four corresponding slots on the inner surface of the sheath and sandwiched between the sheath and a 128-channel curved transvaginal US transducer (central frequency: 6 MHz, 80% bandwidth). A custom-designed 3D printed sheath, shown in Fig. 1(b), was made of

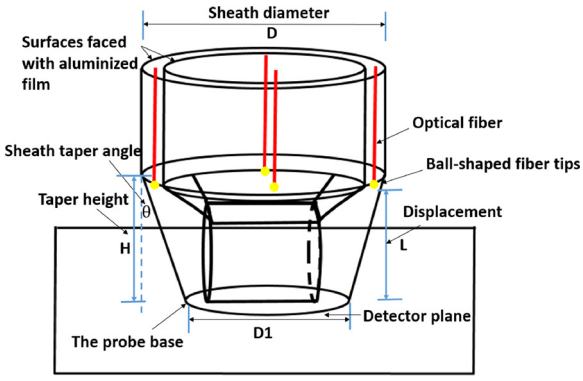

Fig. 2. Model of the imaging probe employed in the simulation, with all design parameters shown. L, fiber displacement; D, sheath diameter; and θ, sheath taper angle. The detector plane is used in Zemax simulation to observe the light fluence.

photopolymer (RGD525). The inner surface of the sheath and the outer surface of the ultrasound transducer were covered with an aluminized film having a reflection coefficient of 85% at 750 nm wavelength.

Four ball lenses (1.5-mm-diameter, n = 1.517, Edmund Optics, N-BK7) were individually glued (Norland Optical Adhesives, Edmund Optics) to the ends of 1 mm core multi-mode optical fibers, as shown in Fig. 1(c).

2.2. Optimization of imaging probe design

Our co-registered US and photoacoustic probe design was optimized to refine its shape and to achieve uniform light homogeneity on the tissue surface, high fluence levels, however, below the ANSI safety limit (~25 mJ/cm^2 in the 700–800 nm wavelength range) [42], and acceptable power output efficiency. Two sets of simulations were performed as described below.

Using a 3D model in Zemax software, the first set of simulations was performed by measuring the subsurface fluence distribution of the four fibers with and without ball-shaped lenses on the fiber tips. The model of the imaging probe, shown in Fig. 2, consisted of two concentric hollow cylinders with diameters of 20 mm and 25 mm, which represented the transvaginal US transducer and the probe sheath, respectively. For the inner cylinder, the front face was a convex

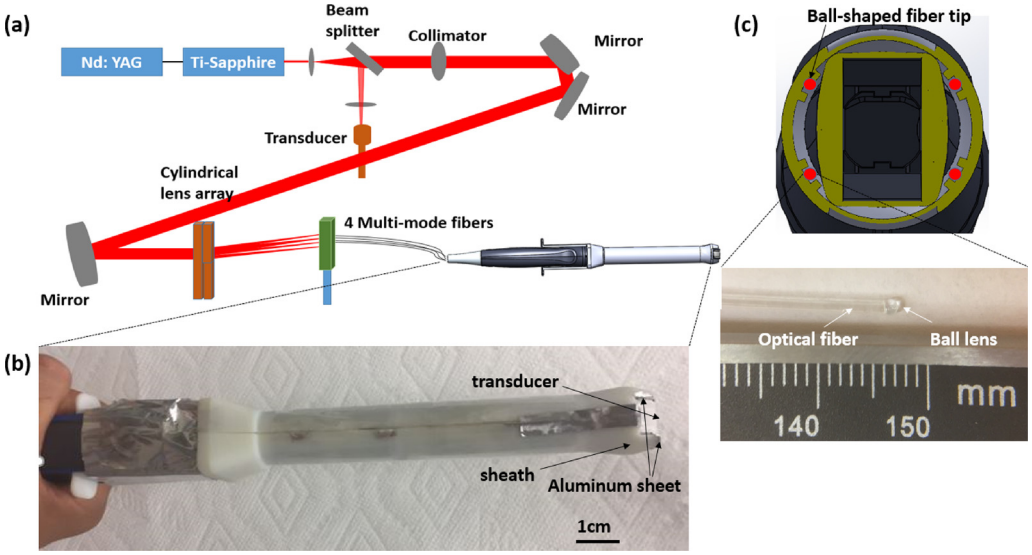

Fig. 1. (a) Light delivery path of PAT/US system. (b) Zoomed-in view of the imaging probe illustrating co-registered PAT/US transducer with cover sheath and transducer inside sheath. (c) Transducer face with four ball-shaped fiber tips (red color). Insert is the enlarged optical fiber with ball-shaped fiber tip.

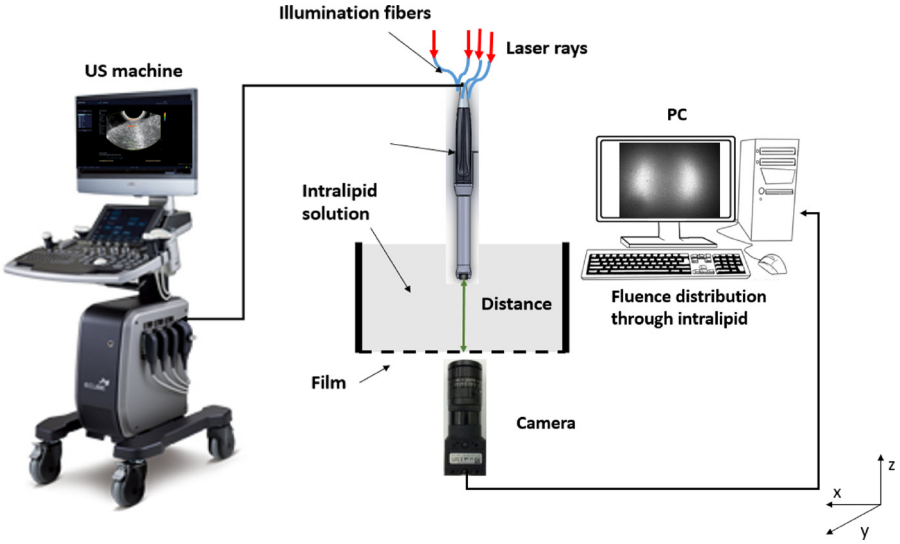

Fig. 3. The experiment setup for measuring the PAT signal from a black thread inside calibrated intralipid solution and recording the light fluence profile. The US system is shown on the left and the detection camera is underneath the intralipid solution with a film to hold the intralipid. The same set-up is also used for measuring PAT signals with the black thread imbedded inside the chicken breast tissue (not show).

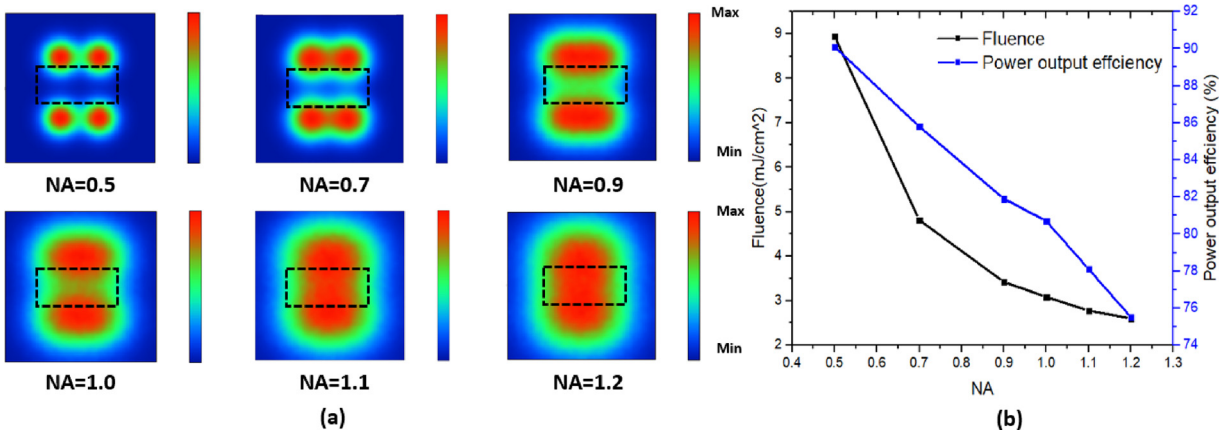

Fig. 4. (a) Simulated fluence profile corresponding to different fiber NA values. The dashed rectangle represents the cross section of the transducer front surface. (b) The laser fluence and power output efficiency corresponding to fiber NAs of 0.5, 0.7, 0.9, 1.0, 1.1, and 1.2.

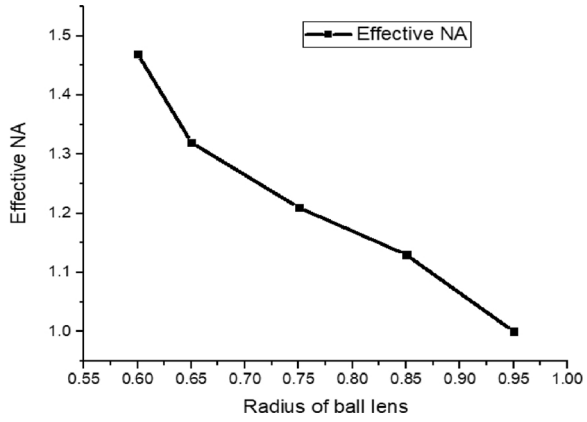

Fig. 5. The relationship between the radius of ball lens and effective NA.

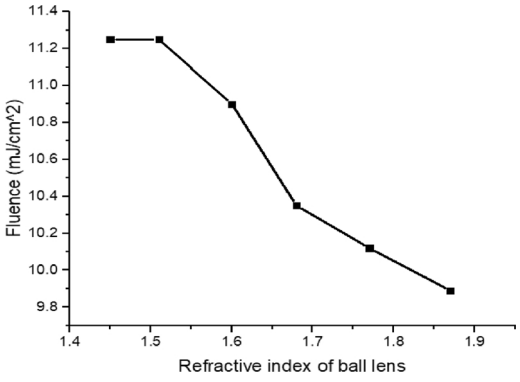

Fig. 6. The laser fluence corresponding to ball lens refractive index of 1.45, 1.51, 1.6, 1.68, 1.77, and 1.87.

curvilinear shape with a rectangular cross-section, representing a typical transvaginal or transrectal transducer front face. The light tunnel formed between the inner surface of the outer cylinder and the outer surface of the inner cylinder was assigned a reflection coefficient of 85% at 750 nm, which is the reflection coefficient of typical aluminized film. The power output efficiency is defined as the ratio of the total energy output from the probe to the total energy exiting the four fibers.

A ball-shaped lens on the fiber tip increases fiber's effective NA. The original fiber's NA was 0.5 without a ball lens, and the ball lens of radius 0.75 mm at the fiber tip increased the NA up to 1.2.

The ball-shaped lens also improved the light fluence, this is due to light refocusing at a short distance in front of the ball lens. The position of the focal point for ball-shaped fibers was calculated using paraxial theory [43–45]: $F = R_{ball}{*}n_{medium}/(n_{ball}\text{-}n_{medium}) = 5.33$ mm, where F is the distance of the distal focal point from the surface of the tip (radius of ball tips, $R_{ball} = 0.75$ mm; refractive index, $n_{ball} = 1.517$) in the medium (refractive index, $n_{medium} = 1.33$). The position of the focal

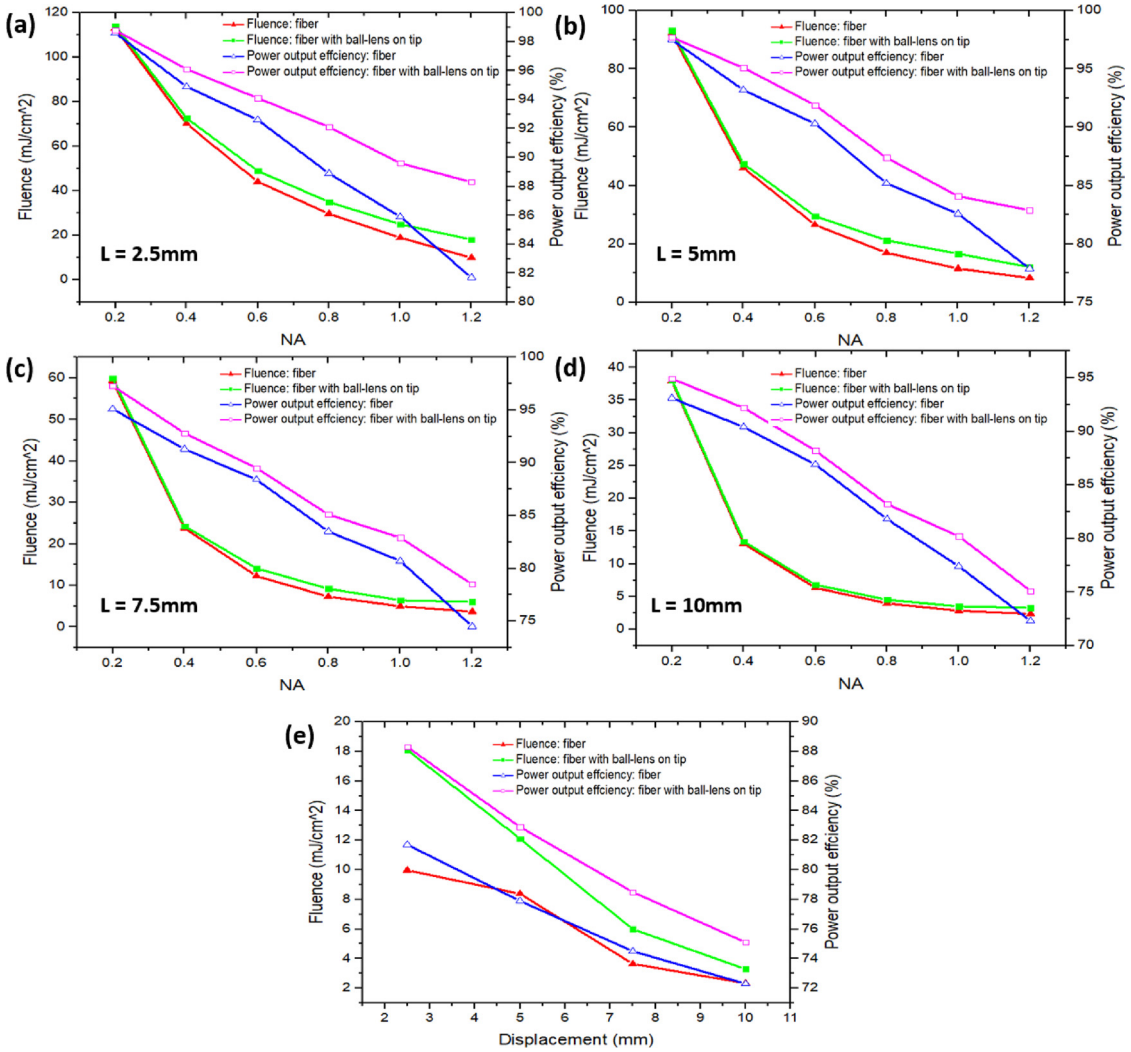

Fig. 7. The laser fluence and power output efficiency for NAs of 0.2, 0.4, 0.6, 0.8, 1.0, and 1.2 and four displacements from the probe base: (a) 2.5 mm, (b) 5 mm, (c) 7.5 mm, (d) 10 mm. (e) The laser fluence and power output efficiency for displacements of 2.5, 5, 7.5, 10 while NA is fixed at 1.2. For all figures, D = 25 mm and the taper angle = 0°.

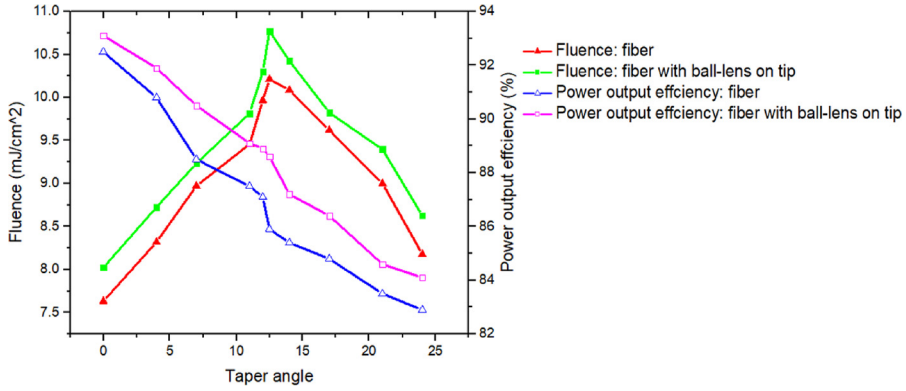

Fig. 8. The fluence and power output efficiency are shown for taper angles of 0°, 4°, 7°, 11°, 12°, 12.5°, 14°, 17°, 21°, 24°. L = 2.5 mm, D = 25 mm, NA = 1.2.

point is related to the radius of the sphere, the refractive index of the medium, and the refractive index of the ball lens.

Several parameters of the imaging probe were investigated in order to obtain light illumination homogeneity and acceptable fluence levels, while at the same time yielding higher power output efficiencies. These parameters, some of which are shown in Fig. 2 include 1) the ball lens refractive index (n); 2) fiber numerical aperture (NA); 3) fiber displacement from the probe tip (L); and 4) sheath taper angle (θ).

The divergence angle of the light exiting the fiber depends on the fiber's NA, which was simulated in Zemax by adjusting the divergence of the light source corresponding to the fiber NA that would give the same divergence. Six different NA, with values of 0.5, 0.7, 0.9, 1.0, 1.1, and 1.2 were simulated.

The focus distance of a ball lens depends on ball lens's diameter,

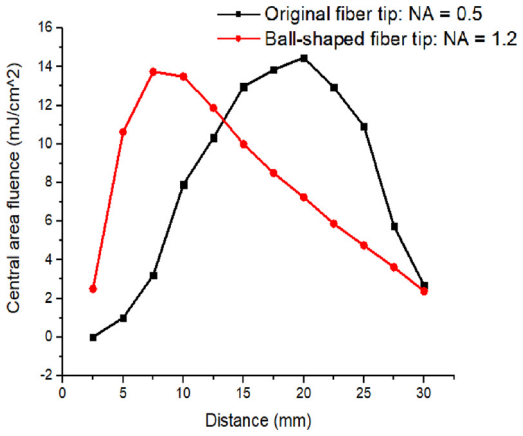

Fig. 9. Simulated fluence in the central imaging area with the original fiber tip and 0.75 mm radius ball-shaped fiber tip, corresponding to detection plane depths from 2.5 to 30 mm, at 2.5 mm intervals.

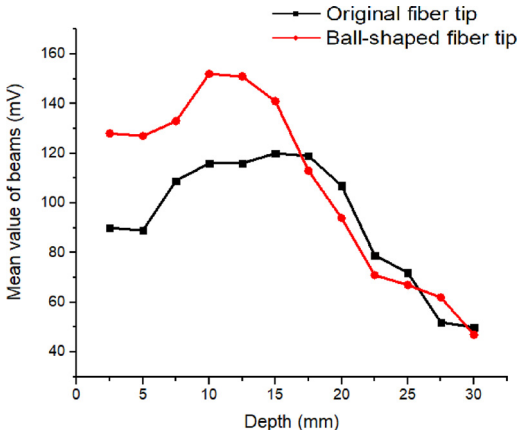

Fig. 10. The experimental laser output power on a 400 μm black thread inside calibrated intralipid solution with the original fiber tip and a 0.75 mm radius ball-shaped fiber tip. Different depths between the fiber tip and the black thread are shown, from 2.5 to 30 mm, at 2.5 mm intervals.

refractive index and the medium refractive index. The converging waist and the diverging angle of the ball lens depend on the ratio between the ball lens diameter and the fiber's diameter [43–45]. The original fiber's NA, refractive index, and diameter were 0.5, 1.4, and 1.0 mm respectively. The ball lens's refractive index was simulated in Zemax by adjusting the material of the lens while keeping the lens diameter fixed at 1.5 mm. Six different refractive indexes, of 1.45, 1.51, 1.6, 1.68, 1.77, and 1.87 were simulated.

The fiber displacement (L) was also varied in Zemax: displacements of 2.5, 5, 7.5 and 10 mm from the probe tip were simulated. For each displacement, the fluence and power output efficiency at the imaging plane were simulated for all the NA values and compared. The simulation results were obtained with the sheath diameter fixed at 25 mm and the sheath taper angle at 0°. The sheath taper angle (θ) was variously set at 0°, 4°, 7°, 11°, 12°, 12.5°, 14°, 17°, 21°, and 24°. These angles were simulated by fixing the taper height (H) at 8 mm and changing D1 from 9 to 12.5 mm, and were simply calculated from the inverse tangent of the ratio (D-D1)/H (Fig. 2). The simulation results were obtained with a beam divergence corresponding to a fiber NA of 1.2 and a displacement of 2.5 mm.

In the second set of simulations, to simulate a muscle wall, the probe was submerged inside a 100 mm deep volume of medium with a reduced scattering coefficient (μ_s') of 4 cm^{-1} and absorption coefficient (μ_a) of 0.02 cm^{-1}. The resulting fluences at twelve different depths from 2.5 mm to 30 mm with 2.5 mm interval were compared. Please note that the depths are defined as the distance from the probe base to the detector plane as shown in Fig. 2.

2.3. Performance evaluation

In order to validate the system performance [46], we conducted five sets of experiments using the setup shown in Fig. 3.

In the first experiment, we evaluated the light delivery efficiency using fibers with ball tips. The performance of the PAT probe with the original fiber tips and ball-shaped fiber tips was compared by measuring the PAT signals coming from a 400 μm diameter black thread parallel to the imaging plane submerged in a water tank filled with calibrated intralipid solution (Fresenius Kabi, USA). We measured signals at 12 different depths, from 2.5 to 30 mm, at 2.5 mm intervals and 780 nm. The intralipid solution had a reduced scattering coefficient (μ_s') of 4 cm^{-1} and an absorption coefficient (μ_a) of 0.02 cm^{-1}.

Next, we evaluated the fluence homogeneity using the ball-shaped fiber tips. We captured the laser fluence distributions at 780 nm at four different depths of calibrated intralipid solution (5, 10, 15, 20 mm), using a 12 bit CCD camera (Basler ace, 30 fps, dynamic range 57 dB), and compared the results with those for the original fiber tips.

Subsequently, we buried sets of 400 μm black threads parallel to the imaging plane inside chicken breast tissue at five different depths, from 5 to 15 mm at 2.5 mm intervals, and imaged them at 780 nm. For each measurement, after coupling gel was applied, the probe was placed in contact with the chicken breast surface. The performance of the PAT probe with the original fiber tips and ball-shaped fiber tips was compared by measuring the PAT signal strengths from the black threads at each depth.

Next, a freshly resected colorectal cancer tissue sample was imaged immediately, after surgical excision from a patient at Washington University School of Medicine. The performance of the PAT probe with the original and ball-shaped fiber tips was compared by measuring the PAT signals at 780 nm, which came from tumor absorption inside the colon sample.

Finally, a palmar vein proximal to the human wrist at a depth of around 1–3 mm and parallel to the imaging plane was imaged in a healthy volunteer. The performance of the PAT probe with the original and ball-shaped fiber tips was compared again by measuring the PAT signals from blood absorption at 780 nm.

3. Results

3.1. Simulation results

Four parameters were sequentially simulated and optimized to test the performance of the endo-cavity illumination design: the fiber's effective NA, the refractive index of the ball lens, the sheath taper angle, and the fiber displacement.

Fiber NA: The effects of using fibers with different NAs on the light fluence are shown in Fig. 4(a). As the NA increases, the maximum fluence and power output efficiency decrease, as shown in Fig. 4(b). However, increasing the divergence of the light exiting the fiber in turn increases the reflection of photons, resulting in a more diffuse and homogenized beam. For ball-shaped fiber tip, 5 different radii of 0.6, 0.65, 0.75, 0.85, 0.95 mm were investigated. The 2D fluence profile and the corresponding 1D profile taken along the horizontal direction were recorded at the detection plane at 7 mm away from the ball-shaped fiber tip. The full width at half maximum (FWHM) after Gaussian fitting of the corresponding 1D profile was used to calculate the ball-shaped fiber tip's NA. Based on the simulation, we selected an NA of 1.2 for the following ball tip design. Calculations showed that a 0.75 mm radius ball tip optimally increased the 1.0 mm diameter fiber's effective NA, from 0.5 to 1.2 as shown in Fig. 5.

Ball lens refractive index (n): The effects of using ball lenses with different refractive indexes on the light fluence are shown in Fig. 6. As

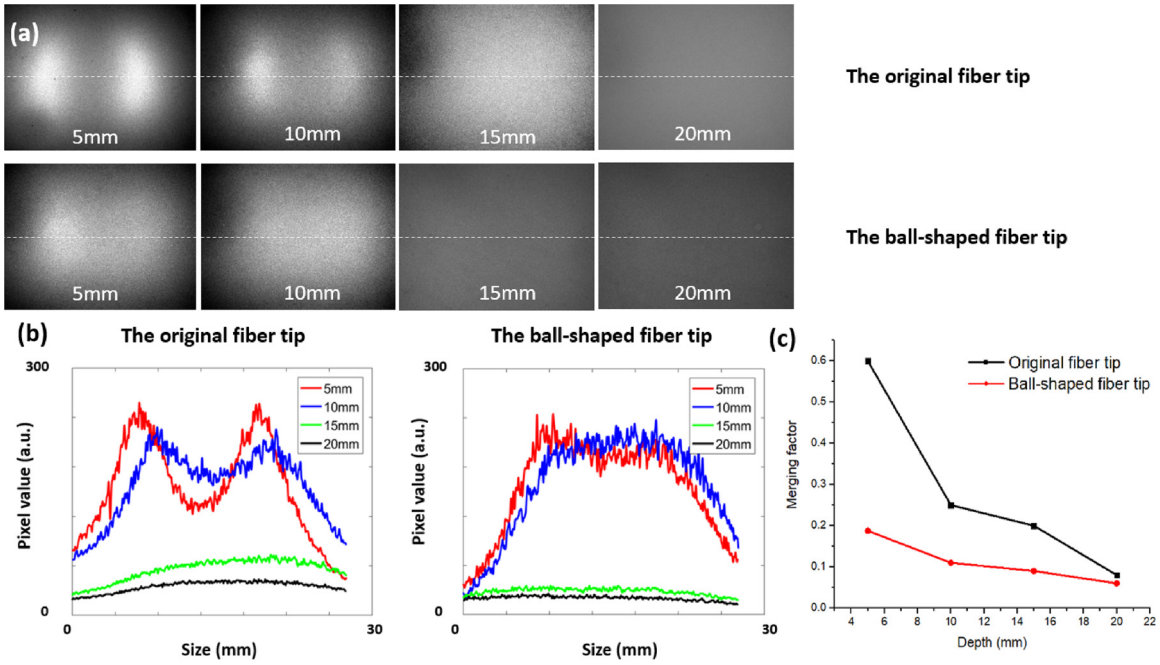

Fig. 11. Experimental light fluence profiles through calibrated intralipid solution corresponding to different distances. (a) The fluence profile pattern through intralipid solution and (b) the corresponding 1D profile taken along the middle intersection in the horizontal direction at thickness of 5, 10, 15, and 20 mm, and (c) calculated merging factor versus depth.

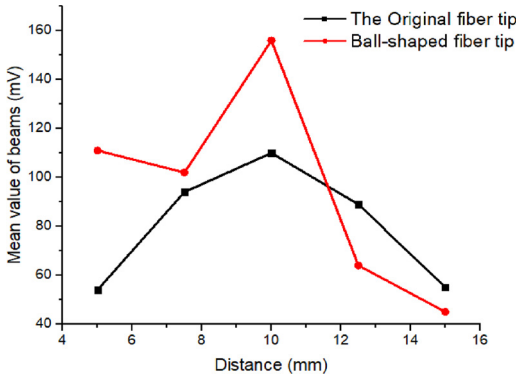

Fig. 12. The experimental laser output power on a set of five 400 μm diameter black threads buried inside chicken breast tissue at depths of 5, 7.5, 10, 12.5 and 15 mm.

the refractive index increases, the light fluence decreases, a consequence of the fiber's refractive index of 1.4. As ball lens' refractive index increases, the mismatch of refractive index between the original fiber and ball lens results in more back scattered light. Based on the simulation, we determined to use n = 1.45–1.52 to be the refractive index range with the highest fluence.

Fiber displacement from probe base (L) and sheath taper angle (θ): For all simulation results, the optimized sheath diameter was fixed at 25 mm, a tolerable size for patients. The effects of using different NA, and displacements on the light fluence and power output efficiency are shown in Fig. 7(a–e). At each of the displacement, as the NA increases, both the power output efficiency and fluence decrease. For NA = 1.2, we chose to use displacement of 2.5 mm to achieve the highest fluence and output power efficiency, as shown in Fig. 7(a). For patient comfort, we do not use displacement less than 2.5 mm. If the fiber tip is too close to the probe base, it can scratch tissue and also create potential hot-spots. Fig. 7(a–e) also show that, compared with a fiber with the same NA, the ball lens provides higher fluence and output power efficiency because of its refocusing properties.

The effects of taper angle on the probe performance are shown in Fig. 8. As the taper increases, the power output efficiency decreases, mainly because the light is increasingly back reflected and scattered. However, for both a ball lens and a fiber with the same NA, the peak fluence increases and then decreases, with a peak value around 12.5°. Note that the fluence output as a function of the probe taper angle is directly affected by the portions of forward and reflected photons. When the taper angles are small, most of the photons are propagating forward through the light tunnel created between the ultrasound probe and the sheath. However, after certain angle, significant portion of photons have reflected back which causes decrease of fluence. Based on simulations, we selected a taper angle of 12.5° to obtain the highest light fluence and acceptable efficiency. Calculations showed that the ball lens could improve the fluence and power output efficiency by 6.46% and 3.14% respectively.

Second set of simulations: In a second set of the simulations, we examined the relationship between the distance of the optical detection plane from the fiber tips and the central area light fluence at the detection plane. Fig. 9 shows the results for an original fiber tip (NA = 0.5, displacement = 5 mm) and a 0.75 mm radius ball-shaped fiber tip (NA = 1.2, displacement = 2.5 mm). At less than 13 mm distance, the central fluence from the ball tip is much higher than that from the original fiber tip, indicating an increased NA and improved light homogeneity. For distances greater than 13 mm, the fluence at the central imaging area underneath the probe of the original fiber setup is higher than with the ball-shaped fiber setup. With the original fiber, the light beam is homogenized by penetrating through the scattering medium, and the lower NA can decrease light scattering events. However, since more photons are scattered when the distance between the fibers and the detection plane increases, the fluence in the central area decreases for both the ball tip setup and the original fiber setup.

3.2. Experimental results

Fig. 10 shows the PAT signals measured from a 400 μm diameter black thread parallel to the imaging plane at 12 different depths inside a water tank filled with calibrated intralipid solution. The average peak

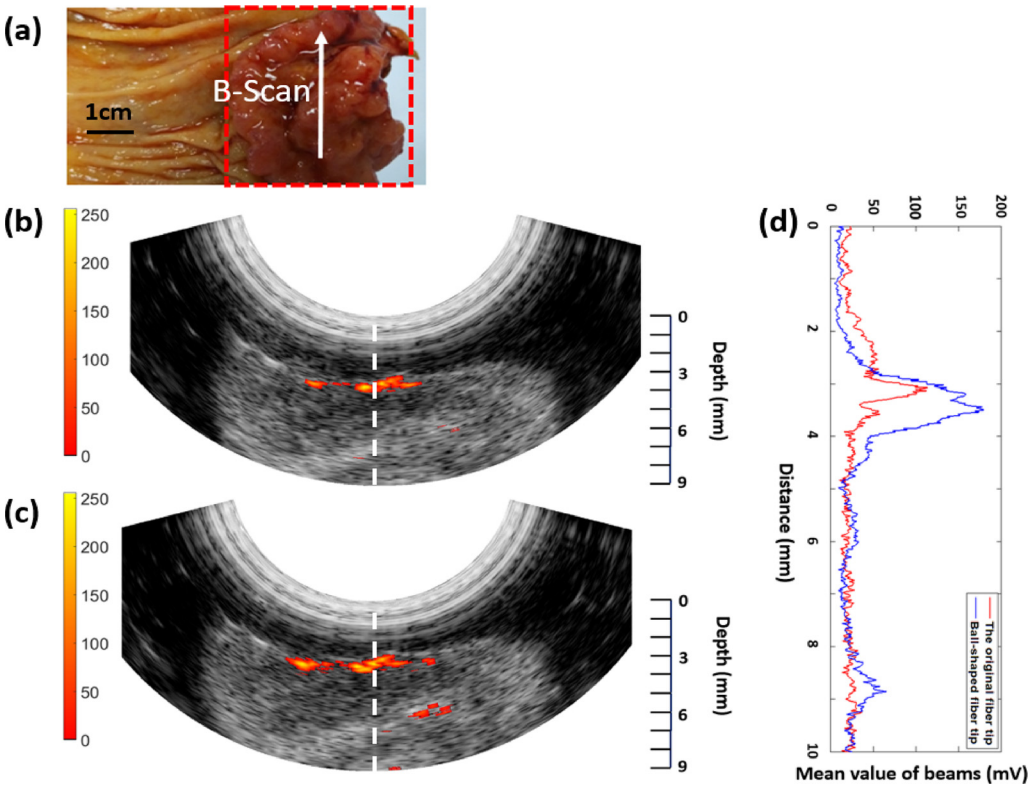

Fig. 13. Color photograph of fresh human colon cancer tissue: (a) the dashed square box outlines the lesion region and the white arrow indicates the direction along which several B-scans were recorded. (b) *Ex-vivo* photoacoustic imaging of human colorectal cancer with the original fiber tip and (c) the ball-shaped fiber tip. (d) Corresponding PAT signals from the same ROI (white dashed line).

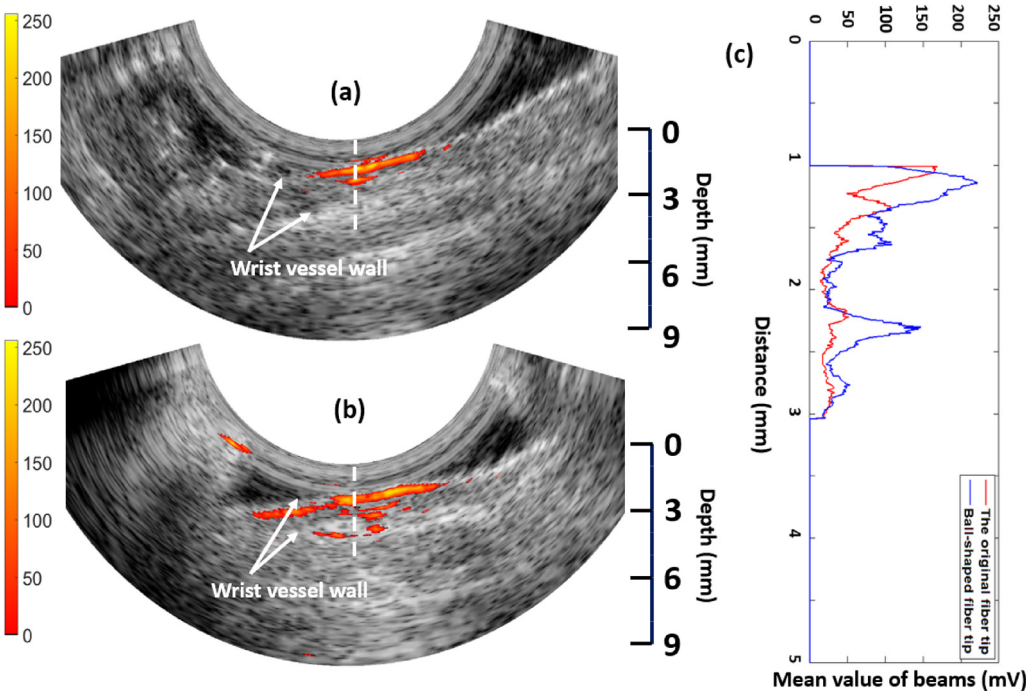

Fig. 14. *In-vivo* photoacoustic imaging of one palmar vein proximal to the human wrist with (a) the original fiber tip and (b) the ball-shaped fiber tip. (c) Corresponding PAT signals from the same ROI (white dashed line).

value of 20 consecutive central beamline envelopes within the region of interest (ROI) was calculated for each distance. For imaging depths shallower than 15 mm, PAT signals from the ball tips are higher than those from the original fiber tips. At depths deeper than 15 mm, the PAT signals from the original fiber tips are higher since the beam is homogenized and the lower NA limits the divergence of the beam and delivers higher fluence. However, as the depth increases, the PAT signals from both tips drops, which is consistent with the previous simulation.

The fluence delivered by the probe after light propagation through 5–20 mm thicknesses of intralipid solution are shown in Fig. 11(a). As the thickness increases, the light fluence distribution from ball tips becomes more uniform than that from the original fiber tip setup, especially up to a thickness of 10 mm. In order to quantitatively

evaluate uniformity, we use a merging factor ($M = \frac{MaxFluence - CenterFluence}{MaxFluence}$) [34] as shown in Fig. 11(b). Compared with the original fiber setup, the ball tips' merging factor is lower for each depth; that is, the beams merge faster and the light fluence distribution becomes more uniform in the photoacoustic imaging. Uniform light illumination over the imaged area is important to obtain an accurate representation of the light absorption map.

The PAT signals coming from a set of 400 μm diameter black threads parallel to the imaging plane and buried inside chicken breast tissue at five different depths are shown in Fig. 12. The average peak value of 20 consecutive central beamline envelopes within ROI was calculated for each distance. At depths shallower than 11 mm, the PAT signals from the ball tips are higher than from the original fiber tips, and at deeper imaging depths, the PAT signals from the original fiber tips are higher. Also, with the increasing depth, the PAT signals in both cases drop, similar to the previous simulation and measurements with the black thread inside intralipid solution. This behavior implies that within an imaging depth of 10 mm, the PAT probe with ball-shaped fiber tips can achieve a higher light delivery efficiency in the central imaging area underneath the probe.

PAT signals from fresh human colorectal cancer tissue, parallel to the imaging plane at around 3 mm depth, were shown in Fig. 13. We note here that this study was approved by Institutional Review Committee and the patient signed an informed consent document. The average peak value of 30 consecutive central beamline envelopes within the ROI was calculated. The PAT signals from the ball-shaped fiber design are higher than the original fiber setup within this depth range. Hence the PAT probe with a ball-shaped fiber tip has a better light delivery efficiency in the central imaging area underneath the probe and transducer, maximizing the sensitivity of the design.

PAT signals coming from a palmar vein proximal to a human wrist, parallel to the imaging plane at around 1–3 mm depth, are shown in Fig. 14. The average peak value of 20 consecutive central beamline envelopes within the ROI was calculated. The PAT signals from the ball tip design are higher than from the original fiber setup within this depth range, which is consistent with the results of the human colon cancer sample.

4. Discussion and summary

This study is evaluating three major parameters: fluence homogeneity and level on tissue surface, and power output efficiency. For lesions on the surface, the fluence homogeneity is a critical parameter to make sure the illumination pattern is uniform with no hot spots. Based on Fig. 4, we choose NA = 1.2. We then consider trade-off between fluence level, power output efficiency and other probe design parameters. For example, we found other optimal parameters such as refractive index n = 1.45–1.52 provided the highest fluence, 2.5 mm displacement provided the highest fluence and output power efficiency. For the taper angle, we choose 12.5° for the highest fluence and relatively high power output efficiency because in this condition, fluence and power output efficiency cannot achieve the highest performance simultaneously.

The proposed ball-shaped fiber tip design increases the fiber's NA, improving light homogeneity and increasing the light delivery fluence on the central imaging area, although there is a decrease in the maximum light fluence on the entire area. Nevertheless, the increased light homogeneity provides acceptable fluence within the ROI under the MPE for patient safety.

In future studies, fabricating the ball-shaped fiber tip directly from the original fiber end, instead of gluing the ball lens to the fiber ends, can yield a more Gaussian laser beam distribution. Moreover, customized micro fiber diffusers [47] can be explored.

The proposed co-registered photoacoustic and ultrasound probe with ball-shaped fiber tips for optimal light delivery has many clinical applications, especially for cancer diagnosis, staging and treatment assessment of surface tumors of internal organs. For example, colorectal cancers start from neoplastic growth from the inner surface of the colon and can penetrate to deeper layers of the colon at late stages. Cervical cancers arise from the cervix and can grow from the surface of the cervix into deeper tissues of the cervix. The cancer may also be growing into the body of the uterus. Accurate diagnosis and staging on cancer invasive depth and repeated assessment of cancer treatment response of these surface cancers are current challenges and research opportunities. The utility of the proposed co-registered photoacoustic and ultrasound probe in these applications will be further explored in the near future.

In summary, we have demonstrated a hand-held endo-cavity photoacoustic/ultrasound probe using ball-shaped fiber tips for noninvasive imaging of human adenocarcinoma. The improved light homogeneity and increased fluence on the central imaged area make the designed probe suitable for *in vivo* noninvasive subsurface tissue imaging.

Conflict of interest

The authors declare that there are no conflicts of interest.

Acknowledgments

This work was supported in part by National Institutes of HealthR01CA151570 and R01EB002136. We gratefully acknowledge the support of Michelle Sperry and June Smith for consenting patients, and pathology resident of Drs. Heba Abdelal and Zahr Alipour for helping with tissue samples, James Ballard for manuscript editing.

References

[1] B.W. Stewart, C.P. Wild, World cancer report 2014, World Health Org. (2014), https://www.who.int/cancer/publications/WRC_2014/en/.
[2] D. Saslow, D. Solomon, H.W. Lawson, M. Killackey, S.L. Kulasingam, J. Cain, F.A.R. Garcia, A.T. Moriarty, A.G. Waxman, D.C. Wilbur, N. Wentzensen, L.S. Downs, M. Spitzer, A.B. Moscicki, E.L. Franco, M.H. Stoler, M. Schiffman, P.E. Castle, E.R. Myers, American Cancer Society, American Society for Colposcopy and Cervical Pathology, and American Society for Clinical Pathology screening guidelines for the prevention and early detection of cervical cancer, Am. J. Clin. Pathol. (2012), https://doi.org/10.1309/AJCPTGD94EVRSJCG.
[3] X. Castellsagué, M. Diaz, S. de Sanjosé, N. Muñoz, R. Herrero, S. Franceschi, R.W. Peeling, R. Ashley, J.S. Smith, P.J.F. Snijders, C.J.L.M. Meijer, F.X. Bosch, M. Plummer, V. Moreno, P. Alonso de Ruiz, S. Chichareon, C. Ngelangel, J. Eluf-Neto, A. Roló, E. Caceres, C. Santos, N. Chaouki, B. El Gueddari, D. Hammouda, T. Rajkumar, Worldwide human papillomavirus etiology of cervical adenocarcinoma and its cofactors: implications for screening and prevention, J. Natl. Cancer Inst. (2006), https://doi.org/10.1093/jnci/djj067.
[4] M.J. Mäkinen, Colorectal serrated adenocarcinoma, Histopathology (2007), https://doi.org/10.1111/j.1365-2559.2006.02548.x.
[5] N. Colombo, S. Carinelli, A. Colombo, C. Marini, D. Rollo, C. Sessa, Cervical cancer: ESMO clinical practice guidelines for diagnosis, treatment and follow-up, Ann. Oncol. (2012), https://doi.org/10.1093/annonc/mds268.
[6] S.P. Raman, Y. Chen, E.K. Fishman, Evolution of imaging in rectal cancer: multimodality imaging with MDCT, MRI, and PET, J. Gastrointest. Oncol. (2015), https://doi.org/10.3978/j.issn.2078-6891.2014.108.
[7] R.A. Kruger, P. Liu, Y.R. Fang, C.R. Appledorn, Photoacoustic ultrasound (PAUS)—reconstruction tomography, Med. Phys. (1995), https://doi.org/10.1118/1.597429.
[8] L.V. Wang, H.-I. Wu, Biomedical Optics: Principles and Imaging, Wiley, New York, 2007.
[9] L.V. Wang, Prospects of photoacoustic tomography, Med. Phys. (2008), https://doi.org/10.1118/1.3013698.
[10] X. Wang, Y. Pang, G. Ku, X. Xie, G. Stoica, L.V. Wang, Noninvasive laser-induced photoacoustic tomography for structural and functional in vivo imaging of the brain, Nat. Biotechnol. (2003), https://doi.org/10.1038/nbt839.
[11] A.A. Oraevsky, A.A. Karabutov, Ultimate sensitivity of time-resolved optoacoustic detection, Proc. SPIE (2000), https://doi.org/10.1117/12.386326.
[12] B.T. Cox, P.C. Beard, Fast calculation of pulsed photoacoustic fields in fluids using *k*-space methods, J. Acoust. Soc. Am. (2005), https://doi.org/10.1121/1.1920227.
[13] A.A. Karabutov, E.V. Savateeva, N.B. Podymova, A.A. Oraevsky, Backward mode detection of laser-induced wide-band ultrasonic transients with optoacoustic transducer, J. Appl. Phys. (2000), https://doi.org/10.1063/1.372127.
[14] G. Ku, X. Wang, G. Stoica, L.V. Wang, Multiple-bandwidth photoacoustic tomography, Phys. Med. Biol. (2004), https://doi.org/10.1088/0031-9155/49/7/018.
[15] L. Yin, Q. Wang, Q. Zhang, H. Jiang, Tomographic imaging of absolute optical

absorption coefficient in turbid media using combined photoacoustic and diffusing light measurements, Opt. Lett. (2007), https://doi.org/10.1364/OL.32.002556.
[16] L. Lin, P. Hu, J. Shi, C.M. Appleton, K. Maslov, L. Li, R. Zhang, L.V. Wang, Single-breath-hold photoacoustic computed tomography of the breast, Nat. Commun. (2018), https://doi.org/10.1038/s41467-018-04576-z.
[17] N. Weidner, J.P. Semple, W.R. Welch, J. Folkman, Tumor angiogenesis and metastasis–correlation in invasive breast carcinoma, N. Engl. J. Med. (1991), https://doi.org/10.1056/NEJM199101033240101.
[18] P. Vaupel, F. Kallinowski, P. Okunieff, Blood flow, oxygen and nutrient supply, and metabolic microenvironment of human tumors: a review, Cancer Res. (1989), https://doi.org/10.1158/0008-5472.can-07-5575.
[19] H.S. Salehi, H. Li, A. Merkulov, P.D. Kumavor, H. Vavadi, M. Sanders, A. Kueck, Ma. Brewer, Q. Zhu, Coregistered photoacoustic and ultrasound imaging and classification of ovarian cancer: ex vivo and in vivo studies, J. Biomed. Opt. (2016), https://doi.org/10.1117/1.JBO.21.4.046006.
[20] T. Wang, Y. Yang, U. Alqasemi, P.D. Kumavor, X. Wang, M. Sanders, M. Brewer, Q. Zhu, Characterization of ovarian tissue based on quantitative analysis of photoacoustic microscopy images, Biomed. Opt. Express (2013), https://doi.org/10.1364/BOE.4.002763.
[21] H. Li, P. Kumavor, U. Salman Alqasemi, Q. Zhu, Utilizing spatial and spectral features of photoacoustic imaging for ovarian cancer detection and diagnosis, J. Biomed. Opt. (2015), https://doi.org/10.1117/1.JBO.20.1.016002.
[22] T. Wang, S. Nandy, H.S. Salehi, P.D. Kumavor, Q. Zhu, A low-cost photoacoustic microscopy system with a laser diode excitation, Biomed. Opt. Express (2014), https://doi.org/10.1364/BOE.5.003053.
[23] V. Neuschmelting, N.C. Burton, H. Lockau, A. Urich, S. Harmsen, V. Ntziachristos, M.F. Kircher, Performance of a Multispectral Optoacoustic Tomography (MSOT) system equipped with 2D vs. 3D handheld probes for potential clinical translation, Photoacoustics (2016), https://doi.org/10.1016/j.pacs.2015.12.001.
[24] L. Song, K. Maslov, K.K. Shung, L.V. Wang, Ultrasound-array-based real-time photoacoustic microscopy of human pulsatile dynamics in vivo, J. Biomed. Opt. (2010), https://doi.org/10.1117/1.3333545.
[25] J. Hui, Y. Cao, Y. Zhang, A. Kole, P. Wang, G. Yu, G. Eakins, M. Sturek, W. Chen, J.X. Cheng, Real-Time intravascular photoacoustic-ultrasound imaging of lipid-laden plaque in human coronary artery at 16 frames per second, Sci. Rep. (2017), https://doi.org/10.1038/s41598-017-01649-9.
[26] P. Wang, T. Ma, M.N. Slipchenko, S. Liang, J. Hui, K.K. Shung, S. Roy, M. Sturek, Q. Zhou, Z. Chen, J.X. Cheng, High-speed intravascular photoacoustic imaging of lipid-laden atherosclerotic plaque enabled by a 2-kHz Barium Nitrite Raman Laser, Sci. Rep. (2014), https://doi.org/10.1038/srep06889.
[27] W. Wei, X. Li, Q. Zhou, K.K. Shung, Z. Chen, Integrated ultrasound and photoacoustic probe for co-registered intravascular imaging, J. Biomed. Opt. (2011), https://doi.org/10.1117/1.3631798.
[28] G.S. Sangha, N.J. Hale, C. Goergen, Adjustable photoacoustic tomography probe improves light delivery and image quality, Photoacoustics (2018), https://doi.org/10.1016/j.pacs.2018.08.002.
[29] C. Kim, T.N. Erpelding, L. Jankovic, L.V. Wang, Performance benchmarks of an array-based hand-held photoacoustic probe adapted from a clinical ultrasound system for non-invasive sentinel lymph node imaging, Philos. Trans. R. Soc. A Math. Phys. Eng. Sci. (2011), https://doi.org/10.1098/rsta.2010.0353.
[30] C. Kim, T.N. Erpelding, L. Jankovic, M.D. Pashley, L.V. Wang, Deeply penetrating in vivo photoacoustic imaging using a clinical ultrasound array system, Biomed. Opt. Express (2010), https://doi.org/10.1364/BOE.1.000278.
[31] B.L. Bungart, L. Lan, P. Wang, R. Li, M.O. Koch, L. Cheng, T.A. Masterson, M. Dundar, J.X. Cheng, Photoacoustic tomography of intact human prostates and vascular texture analysis identify prostate cancer biopsy targets, Photoacoustics (2018), https://doi.org/10.1016/j.pacs.2018.07.006.
[32] Y.-J. Lee, E.-J. Jeong, H.-W. Song, C.-G. Ahn, H.W. Noh, J.Y. Sim, D.H. Song, M.Y. Jeon, S. Lee, H. Kim, M. Zhang, B.K. Kim, Photoacoustic imaging probe for detecting lymph nodes and spreading of cancer at various depths, J. Biomed. Opt. (2017), https://doi.org/10.1117/1.JBO.22.9.091513.
[33] M. Li, C. Liu, X. Gong, R. Zheng, Y. Bai, M. Xing, X. Du, X. Liu, J. Zeng, R. Lin, H. Zhou, S. Wang, G. Lu, W. Zhu, C. Fang, L. Song, Linear array-based real-time photoacoustic imaging system with a compact coaxial excitation handheld probe for noninvasive sentinel lymph node mapping, Biomed. Opt. Express (2018), https://doi.org/10.1364/BOE.9.001408.
[34] P.D. Kumavor, U. Alqasemi, B. Tavakoli, H. Li, Y. Yang, X. Sun, E. Warych, Q. Zhu, Co-registered pulse-echo/photoacoustic transvaginal probe for real time imaging of ovarian tissue, J. Biophotonics (2013), https://doi.org/10.1002/jbio.201200163.
[35] H.S. Salehi, P.D. Kumavor, H. Li, U. Alqasemi, T. Wang, C. Xu, Q. Zhu, Design of optimal light delivery system for co-registered transvaginal ultrasound and photoacoustic imaging of ovarian tissue, Photoacoustics (2015), https://doi.org/10.1016/j.pacs.2015.08.003.
[36] W.A. Benalcazar, W. Jung, S.A. Boppart, Aberration characterization for the optimal design of high-resolution endoscopic optical coherence tomography catheters, Opt. Lett. (2012), https://doi.org/10.1364/OL.37.001100.
[37] X. Li, T.H. Ko, J.G. Fujimoto, Intraluminal fiber-optic Doppler imaging catheter for structural and functional optical coherence tomography, Opt. Lett. (2001), https://doi.org/10.1364/OL.26.001906.
[38] Y. Zhu, N.G. Terry, J.T. Woosley, N.J. Shaheen, A. Wax, Design and validation of an angle-resolved low-coherence interferometry fiber probe for in vivo clinical measurements of depth-resolved nuclear morphology, J. Biomed. Opt. (2011), https://doi.org/10.1117/1.3520130.
[39] V.X.D. Yang, Y.X. Mao, N. Munce, B. Standish, W. Kucharczyk, N.E. Marcon, B.C. Wilson, I.A. Vitkin, Interstitial Doppler optical coherence tomography, Opt. Lett. (2005), https://doi.org/10.1158/0008-5472.CAN-08-1128.
[40] M. Zhao, Y. Huang, J.U. Kang, Sapphire ball lens-based fiber probe for common-path optical coherence tomography and its applications in corneal and retinal imaging, Opt. Lett. (2012), https://doi.org/10.1364/OL.37.004835.
[41] H.S. Salehi, T. Wang, P.D. Kumavor, H. Li, Q. Zhu, Design of miniaturized illumination for transvaginal co-registered photoacoustic and ultrasound imaging, Biomed. Opt. Express (2014), https://doi.org/10.1364/BOE.5.003074.
[42] L.I.A, Laser institute of america, ANSI Z136.1: american national standard for safe use of lasers, SPIE Med. Imaging (2007), https://doi.org/10.1117/12.2043901.
[43] D. Royston, R. Waynant, A. Banks, S. Ramee, C.J. White, Optical properties of fiber optic surgical tips, Appl. Opt. (1989), https://doi.org/10.1364/AO.28.000799.
[44] E. Hecht, A. Zajac, Optics Addison-Wesley, Reading, Mass, (1974).
[45] R.M. Verdaasdonk, C. Borst, Ray tracing of optically modified fiber tips. 1: spherical probes, Appl. Opt. (1991), https://doi.org/10.1364/AO.30.002159.
[46] S. Nandy, A. Mostafa, I.S. Hagemann, M.A. Powell, E. Amidi, K. Robinson, D.G. Mutch, C. Siegel, Q. Zhu, Evaluation of ovarian cancer: initial application of coregistered photoacoustic tomography and US, Radiology (2018), https://doi.org/10.1016/j.jretconser.2010.09.009.
[47] M. Li, B. Lan, W. Liu, J. Xia, J. Yao, Internal-illumination photoacoustic computed tomography, J. Biomed. Opt. (2018), https://doi.org/10.1117/1.JBO.23.3.030506.

Guang Yang received his B.S. in Electrical Engineering from Beijing University of Posts and Telecommunications, China and M.S. in Biomedical Engineering from Tsinghua University, China. He is currently pursuing his Ph.D. in Biomedical Engineering at Washington University in St. Louis, USA. His research interest includes design and development of novel photoacoustic imaging systems for early-stage cancer detection.

Eghbal Amidi received his B.S. in Electrical Engineering from Urmia University, Iran and M.S. in the same major from Iran University of Science and Technology, Iran. He is currently pursuing his PhD in Biomedical Engineering at Washington University in St. Louis, USA. His research interest includes Photoacoustic and ultrasound imaging.

Sreyankar Nandy holds a Ph.D. in Biomedical Engineering from Washington University in St. Louis, USA. In addition, he received his B.S. in Physics from University of Calcutta, India, and M.S. in Physics from Indian Institute of Engineering Science & Technology, India, and M. Tech in Appiled Optics from Indian Institute of Technology, India. His researh interest includes optical coherence tomography and photoacoustic tomography.

Atahar Mostafa is a Ph.D. candidate in the Biomedical Engineering Department at Washington University in St. Louis, USA. He received his B.S. degree in Electrical and Electronics Engineering from the Bangladesh University of Engineering and Technology, Bangladesh and his M.S. degree in Electrical Engineering from the University of Saskatchewan, Canada. His research is focused on ultrasound-guided optical imaging techniques.

Quing Zhu is a professor of the Department of Biomedical Engineering and Radiology at Washington University in St Louis. Professor Zhu is a pioneer of combining ultrasound and near infrared imaging modalities for diagnosis and treatment assessment of breast cancers. Professor Zhu has been named Fellow of Optical Society of American, Fellow of SPIE. Her research interests are cancer detection, diagnosis and treatment assessment using ultrasound-guided diffuse optical tomography, photoacoustic imaging, and optical coherent tomography.